Quantifying particle adhesion to the ureteral walls during peristaltic flow

H. J. Anjum[1] and A. Ali [2]

[1]*Department of Mathematics, COMSATS University Islamabad, 45500 Islamabad, Pakistan*
[2]*Department of Mathematics, COMSATS University Islamabad, Attock Campus, 43600 Attock, Pakistan*

In this paper, we investigate the motion of particle(s) under the action of peristaltic flow. The particle trajectories are simulated by considering sinusoidal peristaltic waves. The fluid flow is governed by a two-dimensional Navier-Stokes equation, whereas for the particle dynamics we use the Basset-Boussinesq-Oseen (BBO) equation. The particle trajectories computed for different characteristic peristaltic flows, that is, trapping flow, augmented flow, and backward flow, show that the net horizontal particle displacement is largest for the augmented flow case. In general, the particle motion depends on its location in the peristaltic channel because of the wall curvature, which directly affects the flow velocities. The reported results for a cluster of particles show that whilst a fraction of particles form a group and propagate along the wave, some particles are left behind that deposit on the channel wall. In many biological processes it is desirable to know the number of particles that accumulate on the channel walls. In the present work, we propose empirical relations which can be used to calculate particle adhesion as a function of time.

I. INTRODUCTION

Peristalsis refers to a fluid transport in an elastic tube undergoing repeated contractions and expansions as a result of peristaltic waves traveling laterally along the tube walls. Peristaltic flows are of particular importance in many of the biological systems where peristalsis is the means of material and fluid transport. For example, the continuous periodic muscular contractions or expansions of ducts propel physiological fluids in living organisms. Other physiological transports include swallowing of food through the esophagus, vasomotion of small blood vessels, movement of spermatozoa in the male reproductive tract, urinary flow through the ureters, embryo transport, and many others [1–5].

The initial studies of peristalsis [6,7] investigated simplified theoretical models, under the assumptions of long wavelength and small Reynolds number. These studies successfully characterized the dynamical attributes of the flow in terms of generated pressure gradients, flow velocities, and inspected qualitative flow characteristics. Extensive follow-up research has been carried out by a number of researchers considering different fluids and analyzing flow through various kind of geometries. A good review on the reported research findings can be found in Refs. [8,9].

It is well established that, in many biological systems, solid objects suspended in a fluid are transported by means of peristalsis, for example, urinary flow in the ureters, movement of spermatozoa [4], movement of medical pills, etc. Kidney stones are formed if there are high levels of calcium, oxalate, cystine, or phosphate in the kidney. These minerals solidify resulting in the formation of crystals or solids which are then pumped out in the ureter. This mixture of fluid and particles, calcium oxalate (CaOx) being the most common one, are then flushed through the urinary system by means of peristalsis. In some cases, the stones grow large in size, and so they must be broken down into small pieces by means of extracorporeal shock wave lithotripsy (ESWL) before they can be flushed out of the urinary system. It is, therefore, very important to understand the dynamics of particles suspended in a fluid under the action of peristalsis.

Hung and Brown [10] performed experimental investigation of particle transport by means of peristalsis in a two-dimensional channel. The effects of flow Reynolds number, particle size, and other relevant flow parameters were discussed in detail. An analytical study, under the assumption of long wavelength, was reported by Srivastava and Srivastava [11]. They studied the fluid phase and particle phase of the model separately. Their research investigations include effects of particle concentration on the flow velocities and the development of backward flow, for some critical pressure gradients. Fauci [12] reports numerical simulation of the two-dimensional peristaltic flow of a Newtonian fluid and investigates the effects of the following on particle transport: the particle diameter, the Reynolds number, and the particle initial location. Jiménez-Lozano *et al.* [8] reported analytical and numerical investigations of peristaltic flow. For the fluid part, they calculated a perturbation solution, whereas a numerical solution was sought for the particle motion. They simulated motion of CaOx particles and bacteria particles in the ureter, assuming particle presence does not affect the fluid flow. It was shown that, for a cluster of particles, some aggregate around the channel walls, whereas a fraction of particles propagate, collectively, along the wave. Other studies investigating the dynamics of particulate suspensions in a peristaltic flow include Refs. [13–16].
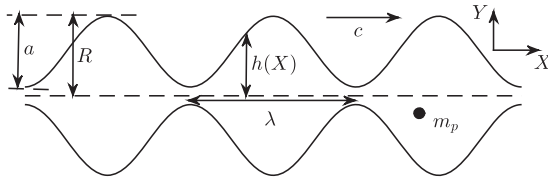
FIG. 1. A schematic diagram detailing the physical and geometric descriptions (picture is not drawn to scale).

As discussed above, understanding the dynamics of particles suspended in a peristaltic flow has many applications in biological processes. The abovementioned studies provide good accounts of particle trajectories and their behavior under different flow conditions; however, there are still some open questions that need to be addressed. As highlighted in Ref. [8] and other studies, particle adhesion to the channel walls has important consequences in the biological context. It is, therefore, important to have a quantitative measure for the particle deposition. We address this problem in the present work and provide an empirical relation to determine the number of particles (as a function of time) adhering to the peristaltic walls. The trajectories of particles and their deposition are discussed for characteristic peristaltic flows, i.e., trapping flow, augmented flow, and backward flow.

There are several modeling approaches for particle laden flows based on the numerical value of the Stokes number $St = \tau_v/\tau_f$, where τ_v is the particle relaxation time and τ_f is some characteristic flow timescale. In the present work, we have assumed one-way coupling $(0 < St < 1)$, i.e., only flow fields affect particle dynamics but not vice versa. One-way coupling is appropriate for dilute suspensions where interparticle spacing is much larger than the particle diameter. The fluid is treated as Eulerian and the particle motion as Lagrangian. The Lagrangian approach for particle tracking is limited in the sense that particle-particle interactions or particles' interaction with the base fluids cannot be captured. Furthermore, for large clusters of particles, the Lagrangian approach can be computationally costly as at each time instant tracking a large number of particles will consume a lot of computational time. The rest of the paper is organized as follows.

In Sec. II, we discuss the mathematical model for the fluid part and the particulate part. Problem schematics, mathematical equations, and assumed physical assumptions are discussed in detail. The results for particle trajectories and particle adhesion are discussed in Sec. III. Finally, in Sec. IV, we draw our conclusions.

II. MATHEMATICAL FORMULATION

In this paper, we study a two-dimensional peristaltic flow of an incompressible Newtonian fluid in a rectangular channel. A schematic diagram showing flow geometry and physical parameters is given in Fig. 1. Although in a medical science context, peristalsis occurs in organs that have axisymmetric geometry, it is shown [6] that the characteristic flow in a planar configuration, one we consider here, exhibits flow features very similar to those of the axisymmetric case. We use the Cartesian coordinate system, taking the X axis along the horizontal direction and the Y axis in the vertical direction. The flow is driven by a peristaltic wave traveling with speed c at the channel boundaries. The amplitude and the wavelength of the wave are denoted by a and λ, respectively. The flow is symmetric about the central axis, fixed at $Y = 0$, and is shown by the horizontal dashed line in the figure. The distance from the wave crest to the central axis is denoted with R, whereas the height of the channel, $h(X)$, represents the distance of the channel boundary from the central axis. m_p is the mass of the submerged particle whose dynamics, under the influence of peristaltic flow, are studied in this paper.

In order to analyze the particle dynamics under the influence of peristaltic flow, we first obtain the solution of the fluid part. A peristaltic flow is unsteady by nature, but can be regarded as steady when viewed in a frame of reference moving with the speed of the wave. This coordinate transformation from the fixed frame (X, Y) to the moving frame (x, y) is given by $x = X - ct$ and $y = Y$. The governing equations, in dimensionless form, for an incompressible Newtonian fluid, in a moving frame of reference, read as follows:

$$u_x + v_y = 0, \tag{1}$$

$$\epsilon \text{Re}(uu_x + vu_y) = -p_x + (\epsilon^2 u_{xx} + u_{yy}), \tag{2}$$

$$\epsilon \text{Re}(uv_x + vv_y) = -\frac{1}{\epsilon^2}p_y + (\epsilon^2 v_{xx} + v_{yy}) - g, \tag{3}$$

where u and v represent the horizontal and vertical velocities, respectively. For the dimensionless equations we use λ/π and R as the horizontal and vertical length scales, and we use c and ϵc as the characteristic horizontal and vertical speed and scale pressure with $\mu c/\epsilon R$, where μ represents kinematic viscosity of the fluid and R is the maximum height of the channel computed from the central axis $(y = 0)$. The dimensionless parameter $\epsilon = R\pi/\lambda$ is the wave number which represents the ratio between the maximum channel height and the wavelength. Re is the Reynolds number $\text{Re} = Rc/\nu$ which gives the ratio between the inertial and the viscous forces. The constant $g = g_0/(\epsilon \nu c/R^2)$ appears due to the gravitational forces $(g_0 = 9.8 \text{ m/s}^2$ represents gravitational acceleration).

For theoretical convenience, we eliminate pressure from Eqs. (2) and (3) by means of cross differentiation and reformulate the resulting model in the stream function $(u = \psi_y, v = -\psi_x)$ form, i.e.,

$$\epsilon \text{Re}(\psi_y \tilde{\nabla}^2 \psi_x - \psi_x \tilde{\nabla}^2 \psi_y) = \tilde{\nabla}^2(\tilde{\nabla}^2 \psi), \tag{4}$$

where $\tilde{\nabla}^2 = \epsilon^2 \partial_{xx} + \partial_{yy}$ represents the (scaled) Laplacian operator. Under the assumption of a long wavelength $(\epsilon \ll 1)$, we seek a perturbation solution of the following form,

$$\psi = \psi^{(0)} + \epsilon \psi^{(1)} + O(\epsilon^2). \tag{5}$$

Substituting the assumed solution form in Eq. (4), we get the following zeroth-order system $[O(\epsilon^0)]$,

$$\psi^{(0)}_{yyyy} = 0, \tag{6}$$

along with the following boundary conditions,

$$\psi^{(0)}(x, 0) = 0, \quad \psi^{(0)}_{yy}(x, 0) = 0, \tag{7}$$

$$\psi^{(0)}(x, h) = q, \quad \psi^{(0)}_y(x, h) = -1, \tag{8}$$

where q is the flux rate in the moving frame of reference, related to the flow rate in the fixed frame, Q, as $Q = q + 1$. In Eq. (8), h represents the channel wall, given below, for the sinusoidal wave form,

$$h(x) = 1 + \phi \sin 2\pi x, \qquad (9)$$

where $\phi = a/R$ represents the ratio between the wave amplitude and the maximum channel height. The first-order system [$O(\epsilon)$] is obtained in a similar way,

$$\psi^{(1)}_{yyyy} = \mathrm{Re}\left(\psi^{(0)}_y \psi^{(0)}_{xyy} - \psi^{(0)}_x \psi^{(0)}_{yyy}\right), \qquad (10)$$

with the accompanying boundary conditions,

$$\psi^{(1)}(x, 0) = 0, \quad \psi^{(1)}_{yy}(x, 0) = 0, \qquad (11)$$

$$\psi^{(1)}(x, h) = 0, \quad \psi^{(1)}_y(x, h) = 0. \qquad (12)$$

The solutions of the zeroth-order problem and the first-order problem are found to be the following:

$$\psi^{(0)} = \left(\frac{3q}{2h} + \frac{1}{2}\right)y - \left(\frac{q}{2h^3} + \frac{1}{2h^2}\right)y^3, \qquad (13)$$

$$\begin{aligned}
\psi^{(1)} = &\frac{\mathrm{Re}h'}{280}\left(3h + 11q + \frac{15q^2}{h}\right)y \\
&- \frac{\mathrm{Re}h'}{280}\left(\frac{8}{h} + \frac{27q}{h^2} + \frac{33q^2}{h^3}\right)y^3 \\
&+ \frac{\mathrm{Re}h'}{40}\left(\frac{1}{h^3} + \frac{3q}{h^4} + \frac{3q^2}{h^5}\right)y^5 \\
&- \frac{\mathrm{Re}h'}{560}\left(\frac{4}{h^5} + \frac{10q}{h^6} + \frac{6q^2}{h^7}\right)y^7.
\end{aligned} \qquad (14)$$

Notice that the Reynolds number, Re, appears in the first-order solution (14); hence, it needs to be chosen in a way that the perturbation solution (5) remains uniformly valid. For all of our simulations, the value of Re is such that $\psi^{(1)}$ remains $O(1)$.

The perturbation solution given by Eq. (5) provides an analytical expression for the Eulerian velocity of the fluid. We use this analytical solution to determine the Lagrangian particle paths by solving the ordinary differential equations of the trajectory. In the present work, we have considered one-way coupling between the fluid and the particles, i.e., the fluid motion affects particle motion and not vice versa. This assumption is only valid for dilute suspensions when the interparticle spacing is more than about 100 times the particle diameter d_p. However for dense suspensions, it becomes necessary to include terms in the governing equation to account for the particle-particle interaction. For studying the particle dynamics, we use the Basset-Boussinesq-Oseen equation (BBO equation), which describes the motion of a small rigid sphere in a nonuniform flow at a relatively low Reynolds number [17,18]. If we denote the fluid velocity vector with $\underline{U}^*$ [computed from the stream function given in Eq. (5)] and the particle velocity vector with $\underline{U}^*_p$, the BBO equation reads

$$\begin{aligned}
m_p \frac{d\underline{U}^*_p}{dt} = &(m_p - m_f)\underline{g}^* + m_f \frac{D\underline{U}^*}{Dt^*} \\
&- \frac{1}{2}m_f \frac{d}{dt}\left(\underline{U}^*_p - \underline{U}^* - \frac{r_p^2}{10}\tilde{\nabla}^{*2}\underline{U}^*\right) \\
&- 6\pi r_p \mu\left(\underline{U}^*_p - \underline{U}^* - \frac{r_p^2}{6}\tilde{\nabla}^{*2}\underline{U}^*\right) \\
&- 6\pi r_p^2 \mu\left(\int_0^{t^*} \frac{\frac{d}{dt^*}\left(\underline{U}^*_p - \underline{U}^*\right)}{\sqrt{\pi \nu(t^* - t')}}dt'\right), \quad (15)
\end{aligned}$$

where g is the gravitational vector acting in the negative Y direction, m_p is the mass of the particle, m_f represents the mass of the fluid having the same volume as that of the particle, r_p is the radius of the particle, μ and ν are the fluid dynamic and kinematic viscosity, respectively, and t^* is the time. Using the dimensionless variables $X = \pi X^*/\lambda$ and $Y = Y^*/R$ and scaling velocities with wave speed c and choosing the characteristic time as $\tau_c = \lambda/\pi c$, the BBO equation in the dimensionless form reads

$$\begin{aligned}
\frac{d\underline{U}_p}{dt} = &\frac{\xi}{\mathrm{St}}\left(\frac{2S}{2S+1}\right)\left(\underline{U} - \underline{U}_p\right) + \frac{3}{2S+1}\frac{d\underline{U}}{dt} \\
&+ \frac{\alpha^2}{40(2S+1)}\frac{d}{dt}\tilde{\nabla}^2\underline{U} + \frac{\alpha^2}{24\mathrm{St}}\left(\frac{2S}{2S+1}\right)\tilde{\nabla}^2\underline{U} \\
&+ \sqrt{\frac{9}{2\pi S \mathrm{St}}}\left(\frac{2S}{2S+1}\right)\left(\int_0^{t^*}\frac{\frac{d}{dt}\left(\underline{U} - \underline{U}_p\right)}{\sqrt{(t - t')}}dt' \right. \\
&\left. + \frac{\left(\underline{U}^{(0)} - \underline{U}_p^{(0)}\right)}{\sqrt{t}}\right) + \left(\frac{2(S-1)}{2S+1}\right)\frac{g_0 \tau_c}{c}\underline{g}, \quad (16)
\end{aligned}$$

where $\underline{U}^{(0)}$ and $\underline{U}_p^{(0)}$ represent the fluid and particle velocities at time $t = 0$. In the above equation $S = \rho_p/\rho_f$ gives the density ratio, St is the Stokes number defined as the ratio between the particle relaxation time $\tau_p = \rho_p d_p^2/18\mu$ and the characteristic fluid time $\tau_c = \lambda/\pi c$, and α represents the ratio between the particle diameter d_p and the maximum channel height R. The parameter ξ is the dynamic shape correction factor which accounts for the deviations, in the drag of nonspherical particles, from the Stokes drag. Hence for a spherical particle $\xi = 1$, whereas for other shapes the values of ξ are estimated by means of experimental observations [19]. In the dimensionless BBO equation, given in Eq. (16), the first term represents the Stoke's drag, the second and third terms give the virtual mass representing the force contribution due to the unsteady nature of the flow relative to the particle, the fourth term gives the Faxén force, the fifth term represents the Basset force, and the sixth term is the buoyancy force due to gravity.

For the instantaneous particle position, we solve Eq. (16), numerically, using the Implicit Euler method. For the numerical integration of the integral appearing in the Basset force term, we use the following approximation [20],

$$\int_0^t (dv/dt)/(t - \tau)d\tau = (v - v^{(0)})/\sqrt{0.5t}. \qquad (17)$$

The dicretized equations read as follows:

$$U_p^{(k+1)} = \frac{U_p^{(k)}}{c_7} + \frac{\Delta t}{c_7}\left[c_1 U^{(k+1)} + c_2\left(\frac{dU}{dt}\right)^{(k+1)} + c_3\left(\frac{d}{dt}\tilde{\nabla}^2 U\right)^{(k+1)}\right.$$
$$\left. + \frac{c_4 U^{(k+1)}}{\sqrt{0.5t^{(k+1)}}} + c_4\left(U^{(0)} - U_p^{(0)}\right)\frac{(1-\sqrt{2})}{t^{(k+1)}} + c_5(\tilde{\nabla}^2 U)^{(k+1)}\right], \qquad (18)$$

$$V_p^{(k+1)} = \frac{V_p^{(k)}}{c_7} + \frac{\Delta t}{c_7}\left[c_1 V^{(k+1)} + c_2\left(\frac{dV}{dt}\right)^{(k+1)} + c_3\left(\frac{d}{dt}\tilde{\nabla}^2 V\right)^{(k+1)}\right.$$
$$\left. + \frac{c_4 V^{(k+1)}}{\sqrt{0.5t^{(k+1)}}} + c_4\left(V^{(0)} - V_p^{(0)}\right)\frac{(1-\sqrt{2})}{t^{(k+1)}} + c_5(\tilde{\nabla}^2 V)^{(k+1)} - c_6\right], \qquad (19)$$

where Δt represents the time step, which is taken to be $\Delta t = 10^{-3}$ in our simulations. The superscripts in the above equations represent the values at time $t^{(k+1)}$. The constants $c_1, c_2, \ldots, c_7$ are defined as

$$c_1 = \frac{\xi}{St}\left(\frac{2S}{2S+1}\right), \quad c_2 = \frac{3}{2S+1}, \quad c_3 = \frac{\alpha^2}{40(2S+1)}, \quad c_4 = \sqrt{\frac{9}{2\pi S St}}\left(\frac{2S}{2S+1}\right),$$

$$c_5 = \frac{\alpha^2}{24 St}\left(\frac{2S}{2S+1}\right), \quad c_6 = \left(\frac{2(S-1)}{2S+1}\right)\frac{g_0\tau_c}{c}, \quad c_7 = 1 + \left(c_1 + \frac{c_4}{\sqrt{0.5t^{(k+1)}}}\right)\Delta t. \qquad (20)$$

The spatial location of the particle is then found numerically by solving $dX_p/dt = U_p$ and $dY_p/dt = V_p$, using the implicit Euler method, which gives

$$X_p^{(k+1)} = X_p^{(k)} + \Delta t U_p^{(k+1)},$$
$$Y_p^{(k+1)} = Y_p^{(k)} + \Delta t V_p^{(k+1)}. \qquad (21)$$

The flow quantities, in terms of U and V, appearing on the right-hand side of Eqs. (18) and (19) are computed exactly, using MATLAB symbolic differentiation, from the stream function (5).

In the present work, we simulate propagation of calcium oxalates in a peristaltic flow. This is motivated by the fact that CaOx mixtures are commonly used for urinal dilutions to prevent calcium renal stone formulation. Furthermore, if the stones are large enough to cause ureteral obstruction, ESWL is performed to break down the stones. A fluid particle mixture is then transported along the ureter. It is reported [21,22] that even after successful ESWL, residue particles sometimes fail to clear, hence causing regrowth. It is reported in the literature [23,24] that for a diluted urine mixture, the diameter of CaOx particles is approximately 10.2 μm and their average density is approximately 1960 kg/m^3. In the present work, we use the two-chain correction factor $\xi = 1.12$. Other particle parameter values are taken as $S = 1.96$, $\alpha = 4.1 \times 10^{-3}$, and St $= 9.997 \times 10^{-7}$. Urine is an aqueous solution with greater than 95% water content; hence, urine characteristics are similar to those of water (density, $\rho = 1000$ kg/m^3; viscosity, $\mu = 0.000\,89$ Ns/m^2). For biomechanical modeling, the ureteral dimensions in an adult human are given as $R = 2.5$ mm, $\lambda = 120$ mm, and $c = 30$ mm/s [25], which gives $\epsilon = 0.0654$ and Re ≈ 85; hence, all of the simulations are performed for this particular value of the Reynolds number.

III. RESULTS AND DISCUSSION

Peristaltic flows (when analyzed in a moving frame of reference) exhibit three characteristic flow patterns [9,26] namely, trapping flow, augmented flow, and backward flow,

depending upon the presence of circulation (usually termed as "bolus") and its spatial extent. In trapping flow, boluses form under the wave crests and their vertical extent is stretched to the central axis; hence, they do not allow any horizontal flow (between the boluses) along the central axis. In an augmented flow, the vertical extent of the boluses is reduced; hence, a (mainly horizontal) flow exists between the boluses. However, in backward flow, no boluses are formed and all the flow is in the backward direction, opposite to that of the wave. Below, we discuss the particle motion in these characteristic flow situations.

Figure 2 shows particle trajectories, for three time periods, i.e., $t = 3T$, in a frame of reference, moving with the speed of the wave. The particle simulations are conducted for Re $= 85$ and $\phi = 0.8$ and at $q = -0.1$ [Fig. 2(a)], $q = 0.1$ [Fig. 2(b)], and $q = -0.7$ [Fig. 2(c)], representing trapping flow, augmented flow, and backward flow, respectively. The channel boundaries are marked using solid black lines, whereas particle trajectories are shown by dashed red lines. The initial locations of the particles are given by the solid circles. For each case, four separate simulations were performed by placing particles under the wave crests ($x = 0.2$, $y = \pm 0.3$) and wave troughs ($x = 0.7$, $y = \pm 0.1$). For trapping flow and augmented flow, shown in Figs. 2(a) and 2(b), respectively, the particles under the wave crests lie in the bolus and hence move in a circulatory fashion. However, the particles under the wave troughs behave differently in each case because of different flow attributes between the boluses, as discussed above. In trapping flow, particles initially located under the wave troughs flow over (and under) the boluses instead of flowing horizontally as in the case of augmented flow. In augmented flow [Fig. 2(b)], particles placed under the wave troughs mainly propagate horizontally, but the trajectories do show a bump corresponding to the region where streamlines are curved indicating the formation of a small vortex besides the main bolus. As for the backward flow, shown in Fig. 2(c), all of the particles move in the direction opposite to that of the wave.
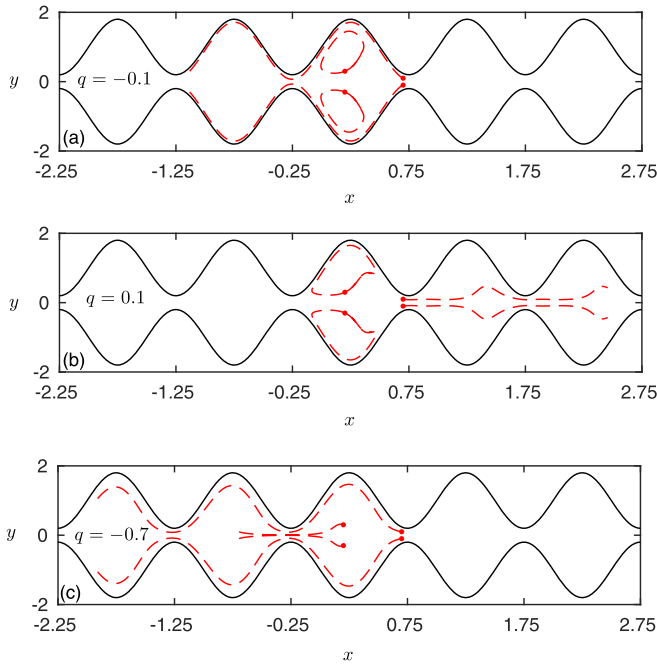
FIG. 2. Particle trajectories viewed in a frame of reference moving with the speed of the wave. The simulations were performed for Re = 85, $\phi = 0.8$, and (a) $q = -0.1$, (b) $q = 0.1$, and (c) $q = -0.7$, representing trapping flow, augmented flow, and backward flow, respectively. The dashed red lines show the particle trajectories traced until $t = 3$, whereas the solid black lines represent the channel boundaries. The initial locations of the particles are given by solid circles.

FIG. 3. Particle trajectories in a fixed frame of reference computed for Re = 85, $\phi = 0.8$, and different values of q. The results for trapping flow ($q = -0.1$), augmented flow ($q = 0.1$), and backward flow ($q = -0.7$) are shown in solid black, dashed red, and dash-dotted green lines, respectively. The solid circular markers on individual curves mark the time interval $T/2$. The results shown in panel (a) represent trajectories of particles that were initially placed under the wave crest (0.2, ±0.3), whereas panel (b) represents trajectories of particles located under the wave troughs (0.7, ±0.1).

In Fig. 3, we show the results from the same simulations as in Fig. 2 but plot the trajectories in a fixed frame of reference. The results corresponding to trapping flow, augmented flow, and backward flow are given by solid black lines, dashed red lines, and dash-dotted green lines, respectively. Figure 3(a) shows the trajectories for particles initially located under the wave crests, whereas the results given in Fig. 3(b) show the trajectories for particles initially placed under the wave troughs. Also shown in Fig. 3(a) is the zoomed view of the particle trajectory, over a specific time period, for the backward flow case. For all of the plotted results, the particle trajectories were computed for three time periods, i.e., $t = 3T$. On each individual curve, solid circles mark the time interval representing a duration of the half time period, i.e., $T/2$. The ticks on the horizontal axis are such that at every full period, i.e., $t = nT$ ($n \in \mathbb{Z}_{\geqslant 0}$), wave troughs are formed at the ticks and at every half period, i.e., $t = (n + 1/2)T$ ($n \in \mathbb{Z}_+$), tick locations correspond to the wave crests.

For trapping flow and augmented flow, particles under the wave crests shown by the solid black line and the dashed red line in Fig. 3(a), rise vertically due to the presence of bolus as seen in Fig. 2. The slight change in the pattern of trajectories is due to the difference in local flow characteristics resulting in different streamline topologies. At $t = 3T/2$, particles reside under the wave crests, close to the channel walls, and hence descend during the wave contraction. This downward propagation is continued for another half period after which the particle continues its motion in a periodic fashion.
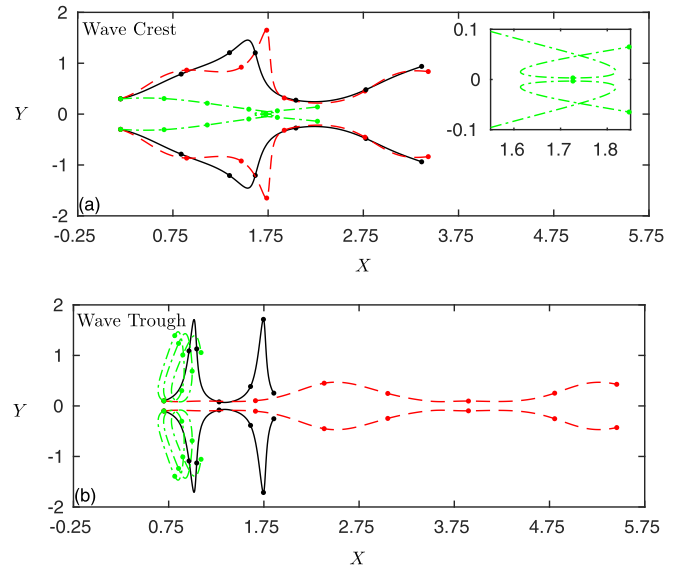
For backward flow, particle trajectory is somewhat different compared to the trajectories of particles in the trapping flow and the augmented flow as discussed above. For backward flow, particles move slowly and remain under the wave crests, close to the central axis, i.e., $Y = 0$, and hence continually descend, vertically, for approximately two periods, reaching wave troughs at $t \approx 2T$. In this region, flow near the channel boundaries is in the positive X direction; hence, due to mass conservation, horizontal flow in the negative X direction exists near $Y = 0$. Therefore, particles propagate in the backward direction (better seen in the zoomed image), showing a slow vertical ascent during the wave expansion and reaching the region where the horizontal flow is positive again; hence, particles continue their vertical ascent whilst moving in the positive X direction.

The mechanism that determines the orientation of the particle trajectory is the topological feature of the channel wall behind the particle. For instance, a particle located on the right of the wave trough experiences upward and rightward force due to the expansion of the wave trough behind the particle. On the other hand, a particle residing on the left of the wave trough experiences downward and rightward force due to the wave crest, behind the particle, undergoing compression. Similar observations are made for particles placed under the wave troughs as shown in Fig. 3(b). It is noticed that trajectories for particles under the wave troughs, in the case of trapping flow and backward flow, mainly exhibit vertical motions due to the fact that they remain under the extreme curved part of the channel. However, in augmented flow, there exists a stream of fluid around the central axis which flows in the horizontal
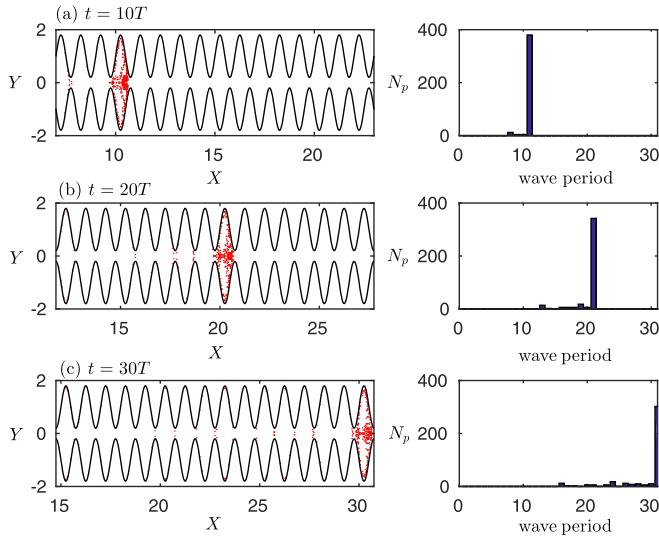
FIG. 4. (Left column) The spatial location of a cluster of 400 particles at time (a) $t = 10T$, (b) $t = 20T$, and (c) $t = 30T$. The red dots show particle locations, whereas black curves mark the channel boundaries. (Right column) The number of particles, present in each wave period at that particular time instant. The simulations are performed for $\phi = 0.8$, Re = 85, and $q = -0.1$ (trapping flow).

FIG. 5. The number of particles in the leading wave column, N_a, plotted as a function of time. The results corresponding to cluster size, $N = 100$, 200, 300, and 400, are shown using black squares, red diamonds, blue circles, and green triangles, respectively. The solid red line, $N_a/N = -0.0101t + 1.058$, is the linear fit to numerical data for $t \geqslant 10$. The simulations are performed for $\phi = 0.8$, Re = 85, and $q = -0.1$ (trapping flow).

direction. It is, therefore, seen that the for augmented flow a particle placed under the wave trough propagates horizontally in contrast to particle trajectories in trapping flow and backward flow. In the above results, we discuss the dynamics of a single particle propagating under the action of a peristaltic flow. We now consider a cluster of equispaced particles and investigate their propagation under different flow conditions.

Figure 4 shows the simulation results for a cluster of 400 particles, initially located in the region $\{-0.1 < X < 0.6, -0.3 < Y < 0.3\}$. The flow parameters are chosen as $\phi = 0.8$, Re = 85, and $q = -0.1$, which represents trapping flow. The plots given in the left column gives the spatial location of particles at $t = 10T$, $t = 20T$, and $t = 30T$. The solid black lines mark the channel boundary, whereas red dots represent the locations of the individual particles. The bar graphs, given in the right column, provide the particle count in individual wave periods where each period represents the section of the wave between two adjacent wave troughs. Notice that, as time evolves, some of the particles are left behind which get stuck to the wall, whereas the remaining particles form a group and detach themselves from the rest of the particles. The detached group of particles continue propagating with the wave as a bolus of particles. This behavior can also be viewed from the bar graphs which give the number of particles present in each column of the wave. It can be seen that the leading column has the most particles followed by a trail of particles left behind in the preceding wave columns. We use the number of particles in the leading column as a quantitative measure for the particle advection by the wave.

In Fig. 5, we plot the number of particles in the leading wave column, N_a/N, as a function of time. The simulations were performed for cluster sizes of $N = 100$ (black squares), $N = 200$ (red diamonds), $N = 300$ (blue circles), and $N = 400$ (green triangles) at $\phi = 0.8$, $q = -0.1$ (trapping flow),
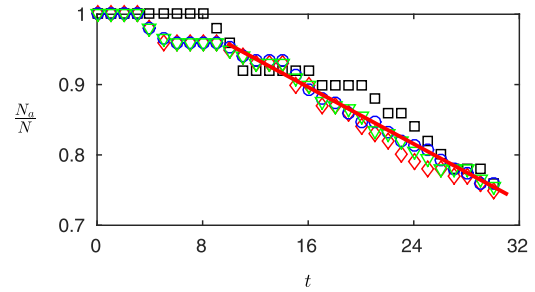
and Re = 85. It is seen that N_a/N shows a decreasing trend in time for $t \geqslant 10$. The results obtained from simulations of different clusters reside very close to each other except for $N = 100$ for which the difference is relatively large. Nonetheless, a decreasing trend is clearly seen for all of the simulation results. A linear fit to the numerical data for $t \geqslant 10$ gives

$$\frac{N_a}{N} = -0.0101t + 1.058, \tag{22}$$

which is shown in Fig. 5 by the solid red line. The empirical result, given above, gives the instantaneous number of particles being advected by the peristaltic wave. The number of particles left behind can be calculated as $1 - N_a/N$, which can be used as a measure for particle deposition, N_d, i.e., $N_d = 1 - N_a/N$. This information is very vital from a biological point of view where particle clearing is intended by means of ESWL. Furthermore, the particles that have grouped together can lead to stone formation under favorable conditions. Bacterial attachment to the inner mucosal tissue can lead to the inflammation of the urethra commonly termed as ureteritis [27].

The simulation results for a cluster of particles propagating in an augmented flow are given in Fig. 6. The simulations are performed for $N = 400$, Re = 85, $\phi = 0.8$, and $q = 0.1$. The particle locations at different time instants are given on the left, whereas the bar graphs on the right provide the particle count in each wave column. The spatial particle location shows a group of particles that form a group that has detached itself from rest of the particles. However, this detached group is spread over multiple wave columns, in contrast to the observations made in the trapping case (Fig. 4) where the detached group resided in the leading wave column. This observation is also confirmed from the bar graphs which show a group of bars (at the leading front) separated from rest of the bars. For the augmented case, it seems appropriate to regard the number of particles in the leading front as a measure for the particle advection N_a. In Fig. 7 we plot N_a/N as a function of time for simulation results corresponding to $N = 100$ (black squares), $N = 200$ (red diamonds), $N = 300$ (blue circles), and $N = 400$ (green triangles) at Re = 85, $\phi = 0.8$, and $q = 0.1$ (augmented flow). It is seen that the number of particle in
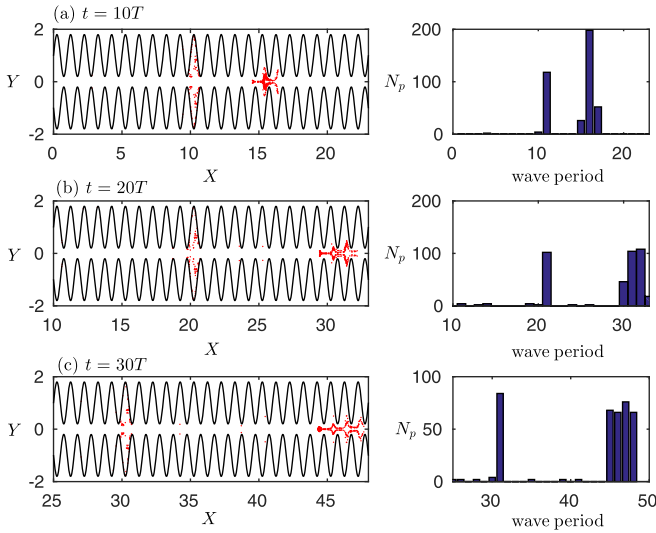
FIG. 6. The simulation results for a cluster ($N = 400$) of particles placed in an augmented flow ($q = 0.1$) at $\phi = 0.8$ and Re = 85. The plots on the left give particle trajectories at times (a) $t = 10T$, (b) $t = 20T$, and (c) $t = 30T$, whereas the bar graphs on the right give the number of particles in each wave period at that particular time instant. The red dots show the spatial location of particles, whereas the black curves mark the channel boundaries.

FIG. 8. The spatial location for a cluster of particles ($N = 400$), in backward flow ($q = -0.7$) at different times. The red dots show particle locations, whereas black curves mark the channel boundaries. The bar graphs on the right give the number of particles, in each wave period. The simulations are performed for $\phi = 0.8$ and Re = 85.

the leading group becomes constant for $t > 5$. A linear fit to the simulation data for $t > 5$ gives

$$\frac{N_a}{N} = 0.6853, \tag{23}$$

which is shown with the solid red line in the figure. The above results show that for augmented flow, the number of particles advected by the wave N_a become constant for large times. This behavior is different from what we observed in the trapping case where N_a showed a decreasing trend in time. The number of particles advected in the augmented case ($N_a/N = 0.6853$) is relatively smaller than the the number of particles advected in the trapping case.

The simulation results for a cluster of particles in a backward flow condition are given in Fig. 8. The simulations are performed for $\phi = 0.8$, Re = 85, $q = -0.7$, and $N = 400$.
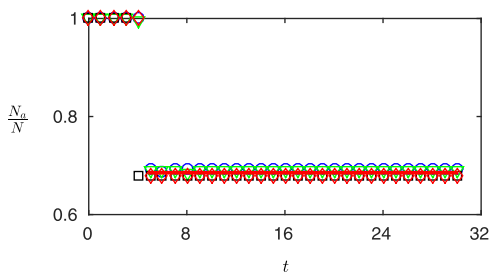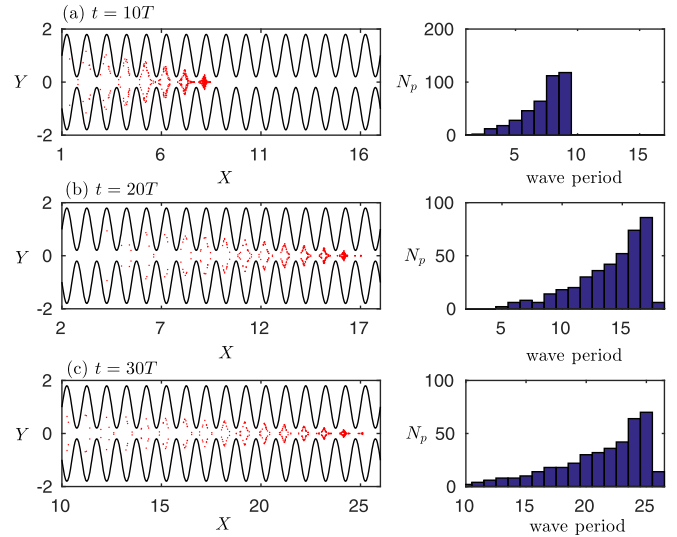

FIG. 7. The number of particles in the leading front, N_a (see discussion), plotted as a function of time. The results corresponding to cluster size, $N = 100, 200, 300$, and 400, are shown using black squares, red diamonds, blue circles, and green triangles, respectively. The solid red line, $N_a/N = 0.6853$, is the linear fit to the numerical data for $t \geqslant 5$. The simulations are performed at Re = 85, $\phi = 0.8$, and $q = 0.1$.

The results on the left give the spatial location of particles, whereas the bar graphs on the right give the number of particles in each wave column. The observations are very different from those for trapping flow and augmented flow. The pattern in the bar graph shows that the particles are continuously left behind, but we are not able to identify any characteristic pattern as in trapping flow or augmented flow. We tried several simulations with different particle sizes and continued simulations until $t = 60T$ but could not identify any specific pattern which can be used to quantify particle advection.

IV. CONCLUSION

Peristaltic pumping of solid particles has many important applications in medical science, for instance, the propagation of medical pills or other medical substances in a human body. Also, kidney stones can develop in the ureter and flow down to the urethra under the action of peristalsis. Motivated by this, we investigate the particle dynamics under the action of peristalsis due to different wave forms. The core objective of this study was to analyze and quantify particle adhesion in the ureter. The phenomenon has been studied previously but a relation which can provide an estimate for the number of particles that accumulate on the peristaltic walls has remained an open question.

To achieve this, we solve the particulate peristaltic problem following the solution methodology of Ref. [28] in which the fluid part is modeled in terms of a two-dimensional Navier-Stokes equation, whereas the particle problem is modeled using a BBO equation, as given in Eq. (16). Our results show that the motion of the particle depend upon its location in the peristaltic channel. This is so because the channel wall has a varying curvature which imposes different amounts of force at different locations during the wave contraction or expansion.

Particle trajectories are computed under different flow conditions for a sinusoidal wave, as given in Eq. (9). The particle propagation is simulated for different characteristic peristaltic flows, i.e., trapping flow, augmented flow, and backward flow. For particles placed under the wave crests, the trajectories for augmented flow and trapping flow are similar as in both cases the particle resides inside a bolus. The net horizontal displacement is largest for particles placed under the wave trough in an augmented flow due to the presence of horizontal flow between the boluses.

Investigating clusters of particles, propagating in trapping flow or augmented flow, it is seen, in agreement with previously reported observations, that a group of particles is formed which propagates with the wave. Whilst this group of particles is advected by the wave, some particles are left behind in the wake, which accumulate on the channel walls. At some point in time, the formed group detaches itself with the rest of the particles and continues forward propagation along the wave. For the trapping case, the group of particles reside in the leading wave column, whereas in the case of augmented flow, the group of particles is spread over a few wave columns.

We denote the number of particles in the group with N_a and regard it as a quantitative measure for the number of particles advected by the wave; hence, $N - N_a$ provides a measure for particle deposition, where N represents the total number of particles. We propose empirical relations, given in Eq. (22) (for the trapping case) and Eq. (23) (for the augmented case), which give the number of particles, N_a, advected by the wave, as a function of time. This can be used to calculate the number of particles that have accumulated on the channel walls. Our results show that the particle deposition, in the augmented case, is relatively larger compared to the particle deposition in the trapping case. For backward flow, particle deposition occurs but we were unable to identify any characteristic pattern which can be used to quantify particle deposition.

This work provides an insight into the dynamics of a particle(s) suspended in a peristaltic flow. The study explains important physical details that affect the motion of particles. Particle adhesion is discussed by computing the trajectories of a cluster of particles. Based on the simulation results, we give an empirical relation to quantitatively measure particle deposition.

[1] J. R. Blake, P. G. Vann, and H. Winet, A model of ovum transport, J. Theor. Biol. **102**, 145 (1983).

[2] O. Eytan and D. Elad, Analysis of intra-uterine fluid motion induced by uterine contractions, Bull. Math. Biol. **61**, 221 (1999).

[3] O. Eytan, A. J. Jaffa, J. Har-Toov, E. Dalach, and D. Elad, Dynamics of the intrauterine fluid–wall interface, Ann. Biomed. Eng. **27**, 372 (1999).

[4] L. J. Fauci and R. Dillon, Biofluidmechanics of reproduction, Annu. Rev. Fluid Mech. **38**, 371 (2006).

[5] G. Kunz, D. Beil, H. Deiniger, A. Einspanier, G. Mall, and G. Leyendecker, The uterine peristaltic pump: Normal and impeded sperm transport within the female genital tract, in *The Fate of the Male Germ Cell*, edited by R. Ivell and A.-F. Holstein, Advances in Experimental Medicine and Biology Vol. 424 (Springer, New York, 1997), pp. 267–277.

[6] A. H. Shapiro, M. Y. Jaffrin, and S. L. Weinberg, Peristaltic pumping with long wavelengths at low Reynolds number, J. Fluid Mech. **37**, 799 (1969).

[7] T. W. Latham, Fluid motion in a peristaltic pump, Master's thesis, Massachusetts Institute of Technology, Cambridge, MA, 1966.

[8] J. Jiménez-Lozano, M. Sen, and P. F. Dunn, Particle motion in unsteady two-dimensional peristaltic flow with application to the ureter, Phys. Rev. E **79**, 041901 (2009).

[9] J. N. Jiménez Lozano, Peristaltic flow with application to ureteral biomechanics, Ph.D. thesis, University of Notre Dame, 2010.

[10] T.-K. Hung and T. D. Brown, Solid-particle motion in two-dimensional peristaltic flows, J. Fluid Mech. **73**, 77 (1976).

[11] L. M. Srivastava and V. P. Srivastava, Peristaltic transport of a particle-fluid suspension, J. Biomech. Eng. **111**, 157 (1989).

[12] L. J. Fauci, Peristaltic pumping of solid particles, Comput. Fluids **21**, 583 (1992).

[13] M. H. Kamel, I. M. Eldesoky, B. M. Maher, and R. M. Abumandour, Slip effects on peristaltic transport of a particle-fluid suspension in a planar channel, Appl. Bionics Biomech. **2015**, 1 (2015).

[14] J. Chrispell and L. Fauci, Peristaltic pumping of solid particles immersed in a viscoelastic fluid, Math. Model. Nat. Phenom. **6**, 67 (2011).

[15] B. Taghilou, M. Pourjafar, and K. Sadeghy, On the use of peristaltic waves for the transport of soft particles: A numerical study, Phys. Fluids **32**, 062108 (2020).

[16] Kh. S. Mekheimer, Peristaltic motion of a particle-fluid suspension in a planar channel, Int. J. Theor. Phys. **37**, 2895 (1998).

[17] M. R. Maxey and J. Riley, Eqnarray of motion for a small rigid sphere in a nonuniform flow, Phys. Fluids **26**, 883 (1983).

[18] C. T. Crowe, J. D. Schwarzkopf, M. Sommerfeld, and Y. Tsuji, *Multiphase Flows with Droplets and Particles* (CRC, Boca Raton, FL, 2011).

[19] W. C. Hinds, *Aerosol technology: Properties, behavior, and measurement of airborne Particles* (Wiley & Sons, New York, 2008).

[20] W. Holländer and S. K. Zaripov, Hydrodynamically interacting droplets at small Reynolds numbers, Int. J. Multiphase Flow **31**, 53 (2005).

[21] M. Shigeta, Y. Kasaoka, H. Yasumoto, K. Inoue, T. Usui, M. Hayashi, and S. Tazuma, Fate of residual fragments after successful extracorporeal shock wave lithotripsy, Int. J. Urol. **6**, 169 (1999).

[22] A. Costa-Bauz, J. Perell, B. Isern, and F. Grases, An experimental study on residual lithiasis after shock wave lithotripsy, Urol. Res. **33**, 51 (2005).

[23] A. Guerra, F. Allegri, T. Meschi, G. Adorni, B. Prati, A. Nouvenne, A. Novarini, U. Maggiore, E. Fiaccadori, and L. Borghi, Effects of urine dilution on quantity, size and aggregation of calcium oxalate crystals induced in vitro by an oxalate load, Clin. Chem. Lab. Med. **43** (2005).

[24] R. C. Walton, J. P. Kavanagh, and B. R. Heywood, The density and protein content of calcium oxalate crystals precipitated from human urine: A tool to investigate ultrastructure and the fractional volume occupied by organic matrix, J. Struct. Biol. **143**, 14 (2003).

[25] S. Boyarsky, C. W. Gottschalk, and E. A. Tanagho, *Urodynamics Hydrodynamics of the Ureter and Renal Pelvis* (Academic Press, New York, 1971).

[26] T. Ehsan, S. Asghar, and H. J. Anjum, Identification of trapping in a peristaltic flow: A new approach using dynamical system theory, Phys. Fluids **32**, 011901 (2020).

[27] P. de Man, U. Jodal, K. Lincoln, and C. S. Eden, Bacterial attachment and inflammation in the urinary tract, J. Infect. Dis. **158**, 29 (1988).

[28] J. Jiménez-Lozano and M. Sen, Streamline topologies of two-dimensional peristaltic flow and their bifurcations, Chem. Eng. Process. **49**, 704 (2010).